

Stress Wave and Phase Transformation Propagation at the Atomistic Scale in NiTi Shape Memory Alloys Subjected to Shock Loadings

Fatemeh Yazdandoost¹ · Reza Mirzaeifar¹

Published online: 21 August 2018
© ASM International 2018

Abstract A unique property of Nickel–Titanium (NiTi) shape memory alloys is their ability to dissipate the shock loading energy by two complementary mechanisms: (a) through deformation-induced phase transformations caused by the structural vibrations, and (b) through the phase transformations caused by the stress wave propagation in the material. Despite extensive research work on the former mechanism, the latter one is still highly unknown, particularly at the atomistic scale. In this paper, the phase transformation, and consequently the energy dissipation, caused by the propagation of stress waves in single-crystal and polycrystalline NiTi alloys under shock wave loadings are investigated using molecular dynamics (MD) method. The nanostructure and dynamic response of the material, when subjected to a shock loading, are studied at the atomistic level. The effects of various nanoscale properties, including the orientation of lattice with respect to the shock loading direction, average grain size, and the effect of grain boundaries on the stress wave propagation, phase transformation propagation, and the energy dissipation in polycrystalline NiTi alloys are studied.

Keywords Nickel–Titanium (NiTi) · Phase transformation · Plastic deformation · Energy dissipation · Shock wave propagation

Introduction

During the past decade, shape memory alloys (SMAs), particularly Nickel–Titanium (NiTi) alloys, have received increasing attention mainly because of their two distinctive properties, the shape memory effect and pseudoelasticity. Both these exceptional properties are based on the inherent capability of NiTi alloys to have two stable lattice structures at different stress or temperature conditions, and the ability of changing their crystallographic structure by a displacive phase transformation between a high-symmetry austenite phase and a low-symmetry martensite phase, in response to either mechanical or thermal loadings [1, 2]. Many novel devices are developed by NiTi alloys in a broad variety of applications such as biomechanical [3], aerospace engineering [4], civil engineering [5], earthquake [6] and shock wave loading conditions [7] and their unique performance relies on either the shape memory effect or pseudoelastic response of NiTi alloys. The pseudoelastic response of NiTi alloys is hysteretic [8–10]. This phenomenon provides ideal energy dissipation and damping capabilities for NiTi alloys and enables them to be used in passive control of structures under earthquake loads [6, 11, 12] or in conditions which materials are subjected to shock waves or high-strain-rate loads [13]. Hence, it is interesting to investigate the energy dissipation in NiTi alloys under shock wave loadings. Despite extensive research work reported on the energy dissipation in SMAs due to quasistatic vibrations, studies on the shock loading and stress wave propagation in NiTi alloys are limited to few researches. Among these, computational methods are prominently used to investigate the energy dissipation, stress wave propagation and phase transformation propagation in SMAs [14, 15], and experimental investigations are barely reported [16–22] due to the limitation of

✉ Reza Mirzaeifar
rmirzaei@vt.edu;
<http://www.me.vt.edu/multismart/>

¹ Department of Mechanical Engineering, Virginia Tech, Blacksburg, VA 24061, USA

measurement devices to capture the complicated transformation and plastic behavior of NiTi alloys at very high-strain-rates loads [14].

Molecular dynamics (MD) method, due to its ability to capture the fundamental details of intrinsic deformation mechanisms at the atomic level, is a superior candidate to study the nano and microstructure and the dynamic response of materials under shock wave loadings. In recent years, the dynamic response of various metals and alloys subjected to shock loading, in absence of phase transformation, have been extensively investigated using MD simulations [14, 23–32]. There have been a number of experimental and computational studies on the dynamic behavior of NiTi alloys subjected to high-strain-rate loadings [33–42]. In a pioneer work, Lagoudas et al. [15] studied the wave propagation problem in a cylindrical polycrystalline NiTi rod induced by an impact loading. In this work, both experimental and continuum based studies (based on a simplified finite element model) have been reported. Despite these studies, there has been only one computational work at the atomistic level which Yin et al. [14] investigated the dynamic behavior and phase transformation of NiTi nano pillars subjected to shock loadings using MD simulations. We have also recently studied dissipation of the energy of cavitation-induced shock waves through phase transformation in NiTi alloys, experimentally and using finite element method [43].

In spite of these computational efforts, there is still a significant gap of knowledge and obvious need to study the fundamentals of dynamic response and behavior of NiTi alloys subjected to shock loadings at the atomistic level. It is well known that the dynamic response of material strongly depends on the nano and microstructural properties such as lattice orientation, grain sizes and grain boundaries. To the best of our knowledge, the effects of these nano- and microstructural properties on the stress wave and phase transformation propagation in NiTi alloys are not studied yet. Therefore, in this paper, the response of single- and polycrystalline NiTi alloys subjected to shock loadings are studied using MD simulations at the atomistic scale, and the effects of lattice orientations, grain boundaries and grain sizes on the shock wave propagation and shock-induced phase transformation propagation are investigated.

Methods

A series of molecular dynamics simulations are performed to investigate the effects of nanostructure on the shock-induced stress wave propagation in NiTi alloys using a many body interatomic potential, originally developed by Lai et al. [44] and subsequently improved by Zhong et al.

[45]. The potential function has been modified with cubic polynomial interpolations to smooth the discontinuities near the cutoff radius. Through multiple case studies, it has been demonstrated that the results of MD calculations are in a good agreement with the experimental results and also ab initio calculations [45, 46]. This potential is adopted in our work. The total potential energy of NiTi is expressed as:

$$E = \sum_i \left\{ \sum_{j \neq i} A_{\alpha\beta} \exp \left[-p_{\alpha\beta} \left(\frac{r_{ij}}{d_{\alpha\beta}} - 1 \right) \right] - \sqrt{\sum_{j \neq i} F(r_{ij})} \right\}, \quad (1)$$

where, the first term in the curly bracket represents the pair interaction between atoms i and j and the second term describes the energy of embedding each atom in the electron cloud of the other atoms. The modified function $F(r_{ij})$ is:

$$F(r_{ij}) = \begin{cases} \frac{r_{ij}^2}{\epsilon_{\alpha\beta}} \exp \left[2q_{\alpha\beta} \left(\frac{r_{ij}}{d_{\alpha\beta}} - 1 \right) \right], & r_{ij} \leq r_1, \\ c_{3,\alpha\beta}(r_{ij} - r_1)^3 + c_{2,\alpha\beta}(r_{ij} - r_1)^2 + c_{1,\alpha\beta}(r_{ij} - r_1) + c_{0,\alpha\beta}, & r_1 < r_{ij} \leq r_c, \end{cases} \quad (2)$$

where parameters α and β represent the element types (here Ni and Ti) of atoms i and j . The distance between atoms i and j is denoted by r_{ij} . The parameters in this potential for describing a NiTi alloy (i.e., values for Ni–Ni, Ti–Ti, and Ni–Ti interaction) have been fitted to the properties of a cubic NiTi system at 0 K [47]. The four coefficients $c_{i,\alpha\beta}$, $i = 1, 2, 3, 4$ are determined by imposing the continuity conditions on $F(r_{ij})$ and its first derivative at r_1 and r_c . The coefficients for this potential have been calculated and reported by Zhong et al. [45] for cutoff radius $r_c = 4.2 \text{ \AA}$.

In the present work, this widely used potential along with large-scale atomic/molecular massively parallel simulator (LAMMPS) [48] is utilized for performing the simulations, and Ovito [49] visualization tool is used for postprocessing the results of MD simulations. The MD simulations are performed for six different 3D computational cells with the average size of $500 \times 500 \times 500 \text{ \AA}$ which are periodic only in x and y directions. In order to simulate the computational cells, three different single crystals with shock directions aligned with $[001]$, $[1\bar{1}1]$, and $[110]$ crystal orientations, and three polycrystalline structures with average grain sizes of 13.5, 18.4 and 25 nm are considered. The single and polycrystalline structures are stabled in the austenite phase. The polycrystalline cells are created using Vorronoi Tessellation algorithm [50]. After creating the single and polycrystalline bulks, the structural energy is minimized using conjugate gradient method. Then, thermal equilibrium is applied to the system using time integration on Nose–Hoover style non-Hamiltonian

equations of motion in canonical (nvt) ensembles to set the temperature at $T = 350$ K for 100 ps. After temperature equilibrium, the system is set to temperature and pressure free using nve ensemble. In order to simulate the shock loading, in a circular area with diameter of 100 \AA , 5 layers of atoms with total thickness of 2.2 nm at the bottom of the bulk system is subjected to the wall/piston [26] loading condition. The wall/piston loading duration is 3 ps with the speed of 7 \AA/ps . Figure 1 shows a single-crystal and a polycrystalline NiTi bulks subjected to the wall/piston loading condition. Finally, after removing the load, the system is equilibrated for 5 ps to let the stress wave propagates through the structure. The results of stress wave propagation and phase transformation, in single crystals with different orientations and also polycrystalline structures with different grain sizes are discussed thoroughly in the following sections.

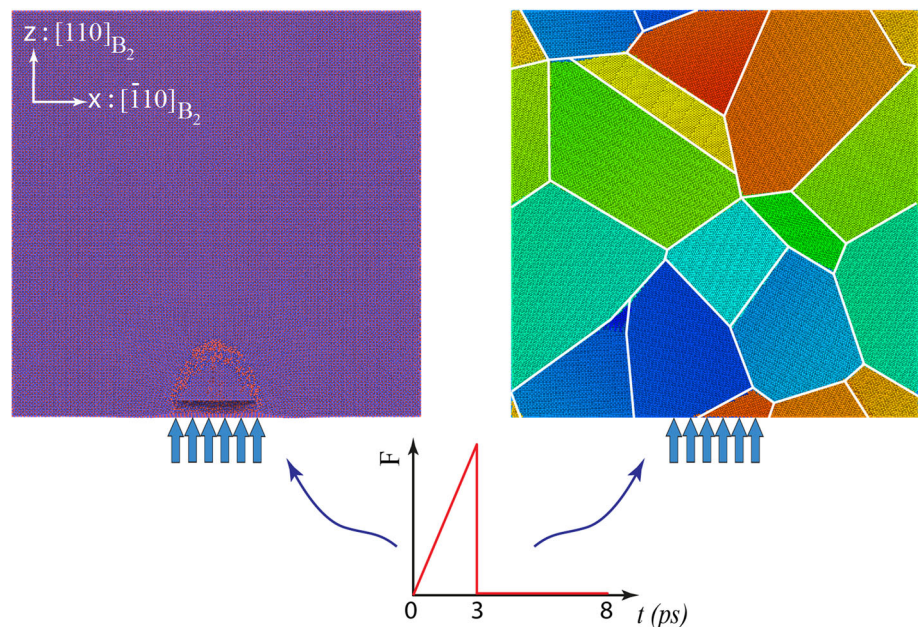
Stress Wave Propagation and Phase Transformation in Different Crystal Orientations

Stress Wave Propagation

In this section, in order to study the effect of lattice orientation on the shock-induced stress wave propagation, three NiTi single crystals with shock loading directions aligned with $[110]$, $[1\bar{1}1]$ and $[001]$ crystallographic directions are simulated. The other two orthogonal directions have been taken as $[\bar{1}10][001]$, $[21\bar{1}][011]$ and $[100][010]$, respectively. The evolution and propagation of the normal and shear stresses in the bulk material are shown in Figs. 2

and 3, respectively. The first two columns in Fig. 2 correspond to the normal stress distribution during the loading and the last three columns represent the stress propagation in unloading (when the shock load is removed as shown schematically in Fig. 1). For all the three single crystals, two shock wave fronts are detected which start to propagate in almost half-circular patterns. The outer circle corresponds to the elastic shock wave front and the inner one represents the inelastic shock wave front, since the elastic shock wave has higher propagation velocity than the inelastic one [7]. As it will be discussed in Section “Interaction Between Plastic Deformation and Phase Transformation”, the inelastic deformation is a combination of permanent plastic deformation and forward austenite to martensite phase transformation. Comparing the three crystal orientations, the elastic wave front which has the magnitude of around -7 GPa is propagated farther in the crystal with the $[1\bar{1}1]$ shock direction. This result was expected since $[1\bar{1}1]$ slip direction has the highest linear density of atoms in body-centered-cubic (BCC) structures, and having closer atoms along this direction promotes the faster propagation of the stress wave. It is well established that, since elastic material constants in an anisotropic material depend on the direction, elastic wave propagation velocity in an anisotropic material also depends on the direction. That is the reason that the shock wave fronts do not show a hemispherical surface. The elastic material constants of austenite NiTi alloy, which is an anisotropic medium, as reported by Brill et al. [51], are $C_{11} = 144$ GPa, $C_{12} = 112$ GPa, and $C_{44} = 22$ GPa. The velocity of the normal mode of elastic stress waves through

Fig. 1 Schematic representation of the single-crystal and polycrystalline bulks subjected to the shock wave loading



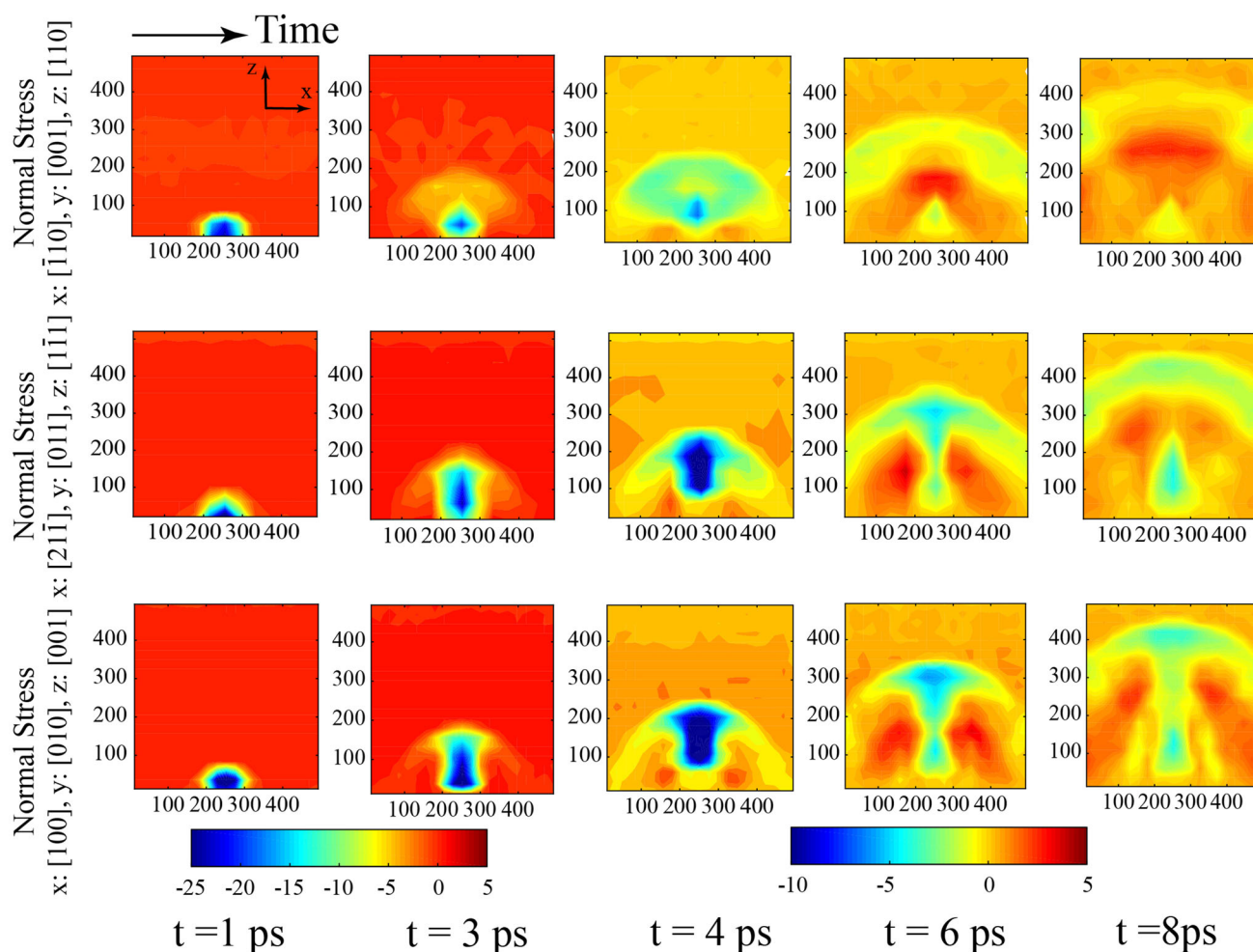


Fig. 2 Normal stress wave propagation of the three single crystals for shock directions aligned with $[110]$, $[1\bar{1}1]$, and $[001]$. The stress values in color bars are in GPa (Color figure online)

the crystallographic directions of $\langle 110 \rangle$, $\langle 1\bar{1}1 \rangle$, and $\langle 001 \rangle$ can be calculated as [52]

$$c_{n\langle 110 \rangle} = \sqrt{1/2\rho(C_{11} + C_{12} + 2C_{44})}, \quad (3)$$

$$c_{n\langle 1\bar{1}1 \rangle} = \sqrt{1/3\rho(C_{11} + 2C_{12} + 4C_{44})}, \quad (4)$$

$$c_{n\langle 001 \rangle} = \sqrt{1/\rho C_{11}}, \quad (5)$$

where, ρ and c_n are density and normal mode elastic wave propagation velocity, respectively. The calculated values of c_n for the three directions are 4804, 4836, and 4707 m/s, respectively. The maximum calculated velocity belongs to the second direction $\langle 1\bar{1}1 \rangle$ which is in agreement with the contour plots of Fig. 2. Right after the onset of unloading, another elastic shock wave initiates and starts to propagate [7]. The unloading wave which is faster than phase transformation wave contributes to the drop in the phase transformation stress peak from -25 GPa to -10 GPa, when it reaches the phase transformation wave front.

A portion of the unloading wave reflects back toward the wall when it hits the inelastic wave front, and then it again reflects back toward the loading direction [7].

As a result of these several reflections, dark orange area in the contour plots of $t = 6$ ps and $t = 8$ ps, where the normal stress is positive, shows the propagation of the unloading elastic wave.

Figure 3 shows the propagation of shear stress waves. Unlike the normal stress waves which initiate and propagate from the circle surface, the shear stress waves initiate from the peripheral of the circle. In a 2D view like Fig. 3, the wave-initiation region appears as a pair of points where in one of them the shear stress is positive and in the other one negative. Similar mechanism as in normal stress wave propagation happens for shear stress wave propagation. The first two columns in Fig. 3 show the initiation steps and the last three columns represent the propagation steps. Due to the different shock source geometries of shear and normal stress waves, the shear stress wave propagation

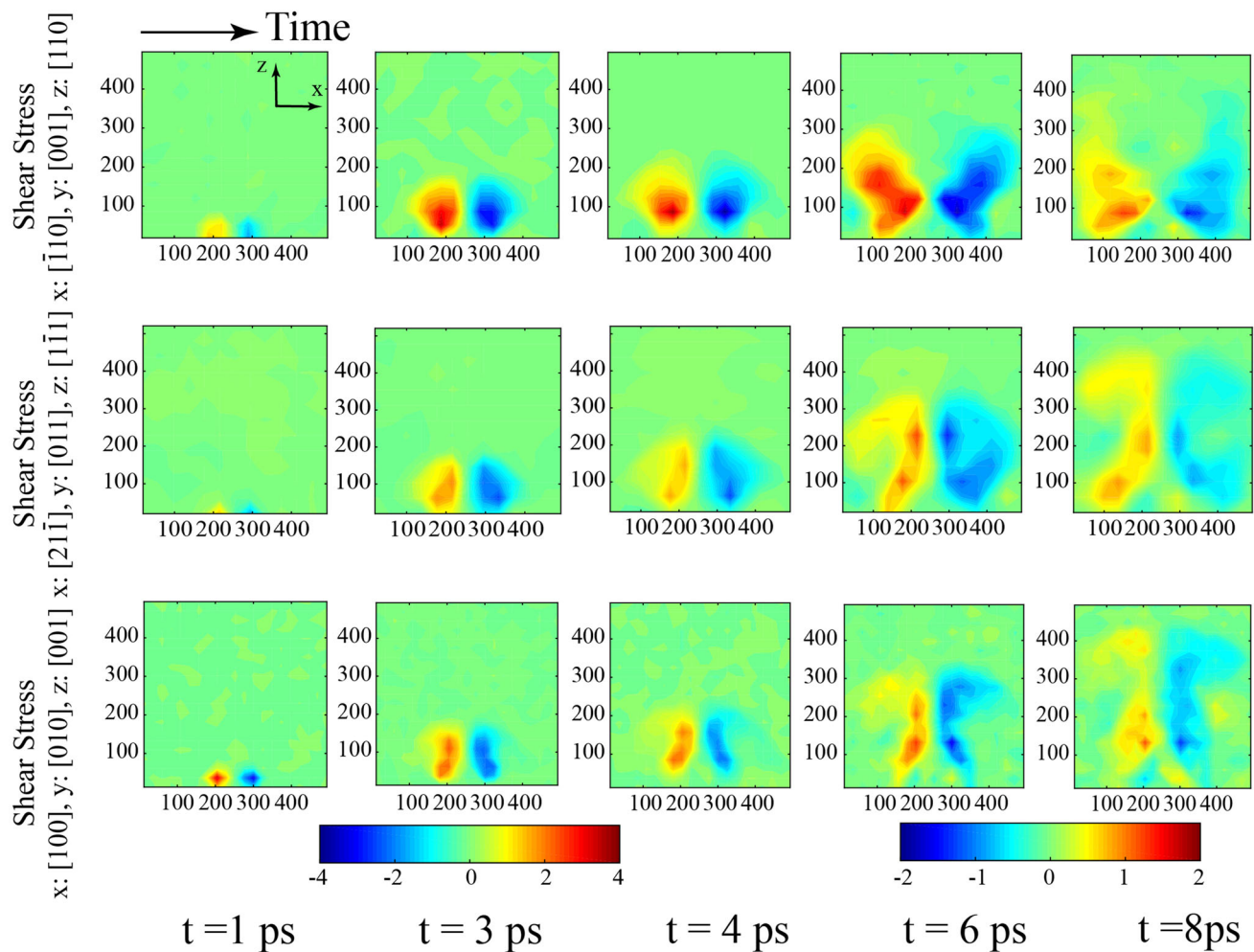


Fig. 3 Shear stress wave propagation of the three single crystals for shock directions aligned with $[110]$, $[1\bar{1}1]$, and $[001]$. The stress values in color bars are in GPa (Color figure online)

pattern appears to be more complicated than the normal stress.

Figure 4 shows the normal stress wave propagation (for convenience, the values of the compressive and tensile stresses are shown positive and negative, respectively) over length for different times in the shock direction. Figure 4a illustrates the evolution of maximum peak stress in the bulk of crystals, for the three orientations, over the time of simulation. The maximum normal stress values for all the crystal orientations show rapid increase shortly after the start of loading. However, for the first orientation, $[110]$, (showing in blue), the maximum stress drops quicker than the other two directions. Right after the end of loading (3 ps) the stress drops at an almost constant rate for all the directions. The curves reach constant values after 6 ps. Figure 4b–d show the distribution of normal stress along the length of the crystals at different times of simulation for the three single crystals with different shock directions $[110]$ and $[1\bar{1}1]$ and $[001]$, respectively.

For the majority of the curves, two distinctive peaks can be observed. The left peak corresponds to the phase transformation shock wave front and the right peak to the elastic shock wave front. As time passes, these two peaks move to the right (the loading direction), but since the elastic wave moves faster than the phase transformation, the two peaks take apart. From the time and locations of these peaks, the shock wave propagation speeds for elastic and phase transformation waves can be calculated for the three crystal orientations. The phase transformation shock wave speeds are calculated as 1229.5, 1025 and 568 m/s, and the elastic shock wave speeds calculated as 5563, 5797 and 5241 m/s for the first $[110]$, second $[1\bar{1}1]$, and third $[001]$ orientations, respectively. The elastic wave speeds calculated from the MD simulations are in agreement with the values calculated from Eqs. (3), (4), and (5). The maximum phase transformation speed is for the shock direction $[110]$, and the maximum elastic wave speed is for the shock direction $[1\bar{1}1]$.

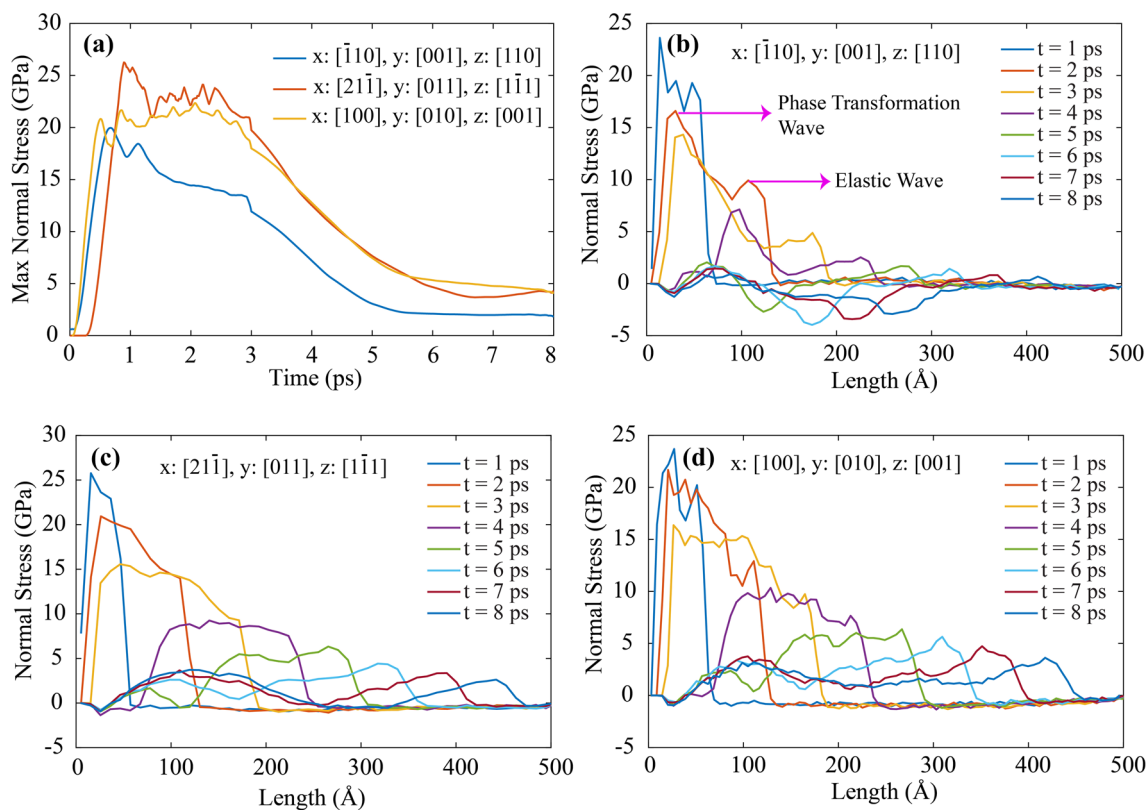


Fig. 4 **a** Maximum values of normal stress waves during loading and propagation times for three different oriented single crystals. **b** Normal stress wave propagation for $x: [\bar{1}10], y: [001], z: [110]$ single crystal.

c Normal stress wave propagation for $x: [2\bar{1}\bar{1}], y: [011], z: [1\bar{1}\bar{1}]$ single crystal. **d** Normal stress wave propagation for $x: [100], y: [010], z: [001]$ single crystal

At the first three curves (1–3 ps), the phase transformation peaks are at high levels (above 14 GPa). This high stress level propagates the phase transformation and plastic deformation through the bulks. Although from 1 to 3 ps some drop in the peak of stress is observed, which could be due to energy dissipation through phase transformation and plastic deformation. However, as discussed before, at the onset of unloading, another elastic wave with an opposite direction starts to propagate at the elastic wave speed. At the time of ~ 4 ps, this unloading wave partially reaches the phase transformation peak and, therefore, causes a significant drop in the stress level. This is why at the time of 5 ps the phase transformation peak drops below 5 GPa for all the directions. This unloading wave then partially reflects back to the wall and again reflects back toward the loading direction. As a combination of these several interactions of unloading elastic wave with the phase transformation wave, this peak drops even more up to the point that for the first orientation, the compressive normal stress drops below zero. Same observation was reported in Ref. [7]. Figure 5 shows the maximum recorded stress values correspond to elastic wave front at different times and their corresponding positions over the length of the crystals, for the

three considered crystal orientations. The calculated stress values are obtained from averaging over the cross sections of the middle cylinder along the loading direction. It can be seen that the third orientation shows the highest stress level and the first orientation the lowest. In Fig. 5, the first crystal shows greater decay in elastic wave front peak compared to the other crystal orientations. To clarify, at the length of 200 Angstrom, the stress in the first orientation drops under 5 GPa, while for the other two directions, the stress level is around 10 GPa. Moreover, as shown in Fig. 4b, the first crystal also shows greater drop in inelastic wave front peak which causes the shortest phase transformation region along the loading direction, and it will be discussed more in the next section.

Phase Transformation Propagation

For an austenite NiTi alloy to transform to a B19' martensite phase, a specific strain condition is needed. The deformation matrix which defines the required deformations of phase transformation from austenite phase to martensite phase is called deformation gradient matrix F . The deformation gradient matrix is calculated for the martensitic phase transformation from B2 austenite phase

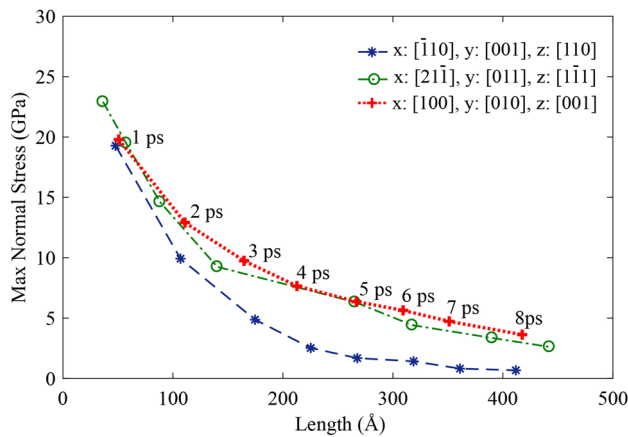


Fig. 5 Decay of normal stress wave for the three single crystals with shock directions aligned with $[110]$, $[1\bar{1}1]$, and $[001]$

to B19' martensite phase of NiTi alloys [45, 53] and using this matrix, the Lagrangian strain matrix can be calculated which gives the required strain components for martensitic phase transformation. The Lagrangian strain matrix of atom i is expressed as [54]:

$$\eta_i = \frac{1}{2} (F_i F_i^T - I) \tag{6}$$

In order to detect inelastic deformations, Von Mises shear strain definition is utilized [14]. This strain condition which is a good measure of local inelastic deformation can be expressed as [54]:

$$\eta_i^{\text{Mises}} = \sqrt{\left(\eta_{yz}^2 + \eta_{xz}^2 + \eta_{xy}^2 + \frac{(\eta_{yy} - \eta_{zz})^2 + (\eta_{xx} - \eta_{zz})^2 + (\eta_{xx} - \eta_{yy})^2}{6} \right)} \tag{7}$$

Using the required Lagrangian strain matrix for martensitic phase transformation, the threshold value of η_i^{Mises} is calculated as 0.11, which is also compatible with the reported value in [55]. The regions correspond to this value of Mises shear strain will have a completed phase transformation to martensite, any region with an equivalent shear strain above this threshold, could have a combination of phase transformation and plastic deformation. Von Mises strain distribution in the three crystal orientations were calculated and shown in the contour plots of Fig. 6. The green colored regions are just above 0.11 and the red colored areas correspond to the strain levels of 0.2 and above. These regions in the plots show the atoms which have a combination of plastic deformation and phase transformation.

Comparing the contour plots of $t = 4$ ps and $t = 8$ ps, it can be seen that some areas are green first, but they return to blue at the end. These regions are the areas in which the forward phase transformation has propagated with no plastic deformation, and the phase transformation has been

reversed back to austenite. The remaining areas, which has not returned back to austenite at the end of $t = 8$ ps, are either martensite regions which need more time to recover to austenite, or the regions in which have experienced a plastic deformation during the stress wave propagation. If the simulation is extended to a very long time, the remaining areas with pure plastic deformation and phase transformations can be distinguished, as the martensite areas will transform back to austenite and the equivalent strain will become zero, while the plastic regions will hold a nonzero strain. More details about this phenomenon are given in Section “Interaction Between Plastic Deformation and Phase Transformation”.

The difference in the contours of the three different orientations is due to the difference in their shear stress wave propagation patterns shown in Fig. 3. The contour plots of Fig. 3 are almost coinciding with the contour plots of Fig. 6, revealing that phase transformation and plastic deformation in NiTi are prominently governed by shear stress, which means when the shear stress in slip planes reaches the critical value, slip happens and those affected regions are permanently deformed. Moreover, when a defect such as plastic deformation is generated in the structure, it can be a trigger for phase transformation propagation. Therefore, we can say that those red-colored regions show the plastic deformation due to slippage on slip planes and also they show the phase transformations which happen due to the presence of the defects.

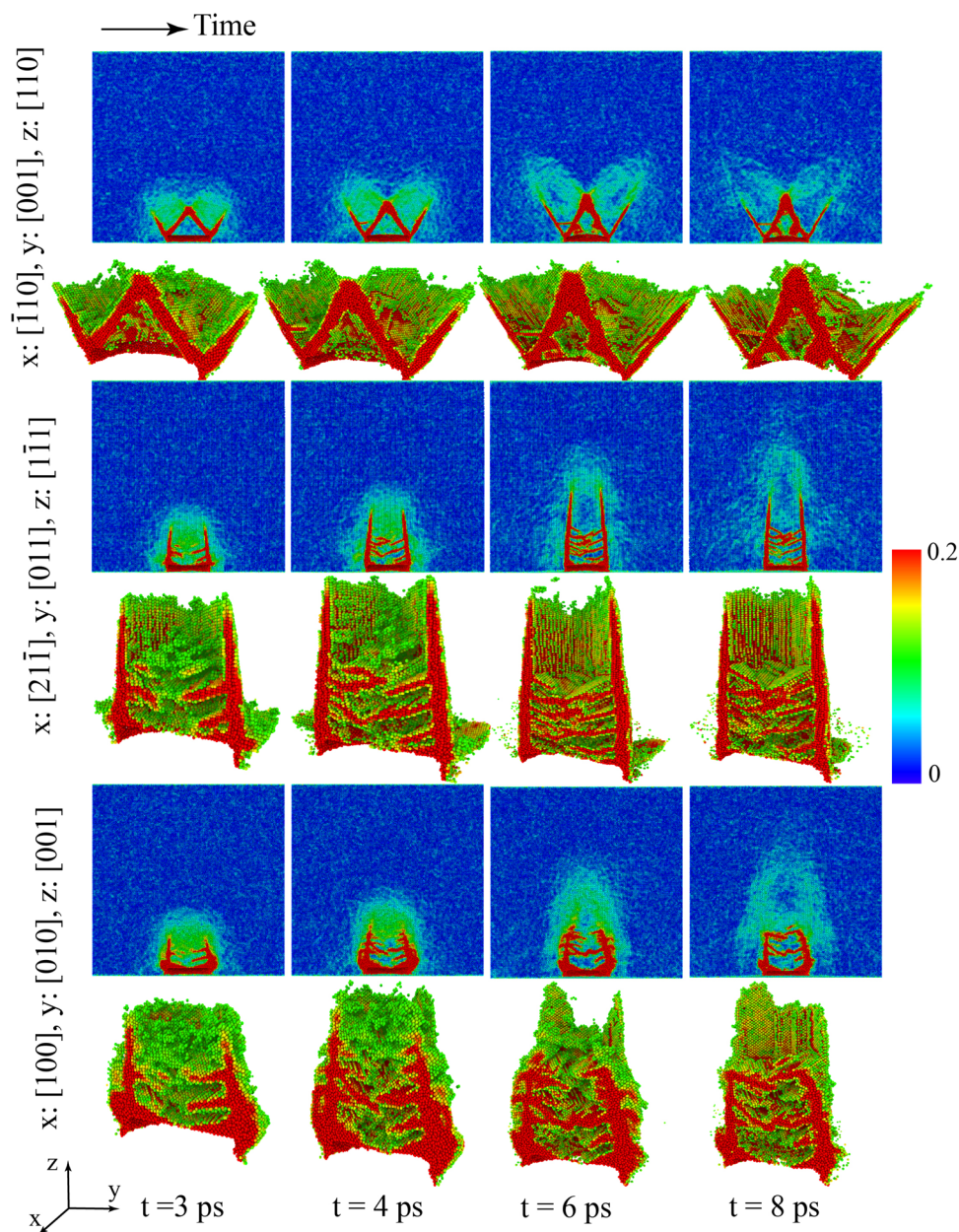
That’s the reason that we see some of the red colored regions returned to blue at the end of the simulation. In Section “Interaction Between Plastic Deformation and Phase Transformation,” we will study the most favorable slip systems of the single crystals with $x : [100]y : [010]z : [001]$ as a representative crystal structure and we will investigate the activated slip systems due to the shock loading. Furthermore, we will propose a method to distinguish the plastic deformation and phase transformation in the structure under shock loading.

Interaction of Stress Wave and Phase Transformation Propagation with the Grains in Polycrystalline NiTi

Stress Wave Propagation

In order to study the effect of grain sizes on the stress wave propagation, three polycrystalline NiTi with different average grain sizes of 13.5 nm, 18.4 nm, and 25 nm are simulated. It is worth noting that the selected size of grains, which actually represent nanocrystalline material, is due to the restrictions in using MD simulations for large systems.

Fig. 6 Von Mises shear strain parameter which shows phase transformation propagation and plastic deformation in three different oriented single crystals under shock loading. Von Mises shear strain values 0 and 0.11 correspond to regions with austenite and martensite phases, respectively. The values between 0.11 and 0.2 show regions with combined phase transformation and plastic deformation



However, it is expected that the fundamental findings will be expandable to polycrystalline structures with larger grain sizes, with an acceptable accuracy.

The evolution and propagation of the normal and shear stresses in the bulks are shown in Figs. 7 and 8, respectively. As it is mentioned in the previous section, the first two columns correspond to the stress distribution during the loading and the last three columns correspond to the stress distribution after removing the shock loading. In Fig. 7 for all the three polycrystalline structures, two shock wave fronts are initiated and started to propagate in almost half-circular patterns, same as the single crystals. The outer circle corresponds to the elastic wave front and the inner one represents the inelastic shock wave front, since the

elastic shock wave has higher propagation velocity than the inelastic one. Right after the removing the shock loading, the unloading elastic shock wave initiates and starts to propagate. The unloading wave which is faster than phase transformation wave contributes to the drop in the phase transformation stress peak from -25 GPa to -10 GPa, when it reaches the phase transformation wave front, dark red area in the contour plots of $t = 6$ ps and $t = 8$ ps, where the normal stress is positive, shows the propagation of the unloading elastic wave. Comparing the stress wave propagations in three different polycrystalline structures, it can be seen that the drops of shock wave fronts increases by decreasing the grain sizes. Moreover, by decreasing the grain sizes, the grain boundaries volume fraction in the

bulk structures is increased and these grain boundaries not only damp the stress shock wave propagations, but also cause many reflections of shock stress waves. Since, in fine grain sizes the volume fraction of grain boundaries increases, then they can damp the stress waves more compare to the coarse grain sizes.

Figure 8 shows the propagation of shear stress. The shear stress wave initiates at the peripheral of the cylinder which is a circle. In a 2D view like Fig. 7, the wave initiation region appears as a pair of points where in one of them the shear stress is positive and in the other one negative, same as single crystals. It can be seen that the shear stress wave front decreases after $t = 4$ ps when it reaches the first grain boundary in the shock direction and similar mechanism as normal stress wave propagation happens for the shear stress wave propagation in polycrystals.

Figure 9a illustrates the evolution of maximum peak stress in the polycrystalline NiTi, for the three grain sizes, over the time of simulation. The maximum normal stress values for all the grain sizes shows almost the same trend.

However, during the loading it can be seen that, on average, the normal stress decrease by decreasing the size of grains. It is worth noting that at the very beginning of the loading, the stress peaks strongly depend on the impact velocity and temperature, and are almost the same. From another point of view, at late stages of loading, the reflected waves can also affect the maximum stress waves. In addition to these, the inevitable uncertainties of MD results should also be considered. Therefore, making a concrete conclusion is not possible, but instead we try to use the average values to make acceptable conclusions on this topic. As it is mentioned in the previous section, this can be due to increasing the volume fraction of grain boundaries in the bulk structure and the reflections from grain boundaries. These grain boundaries act like an obstacle for stress wave fronts in the shock direction. Figure 9b–d show the distribution of normal stress along the length of the bulk structures at different times of simulation for the three different grain sizes. At the first three curves (1–3 ps), the phase transformation peaks are at high levels (above

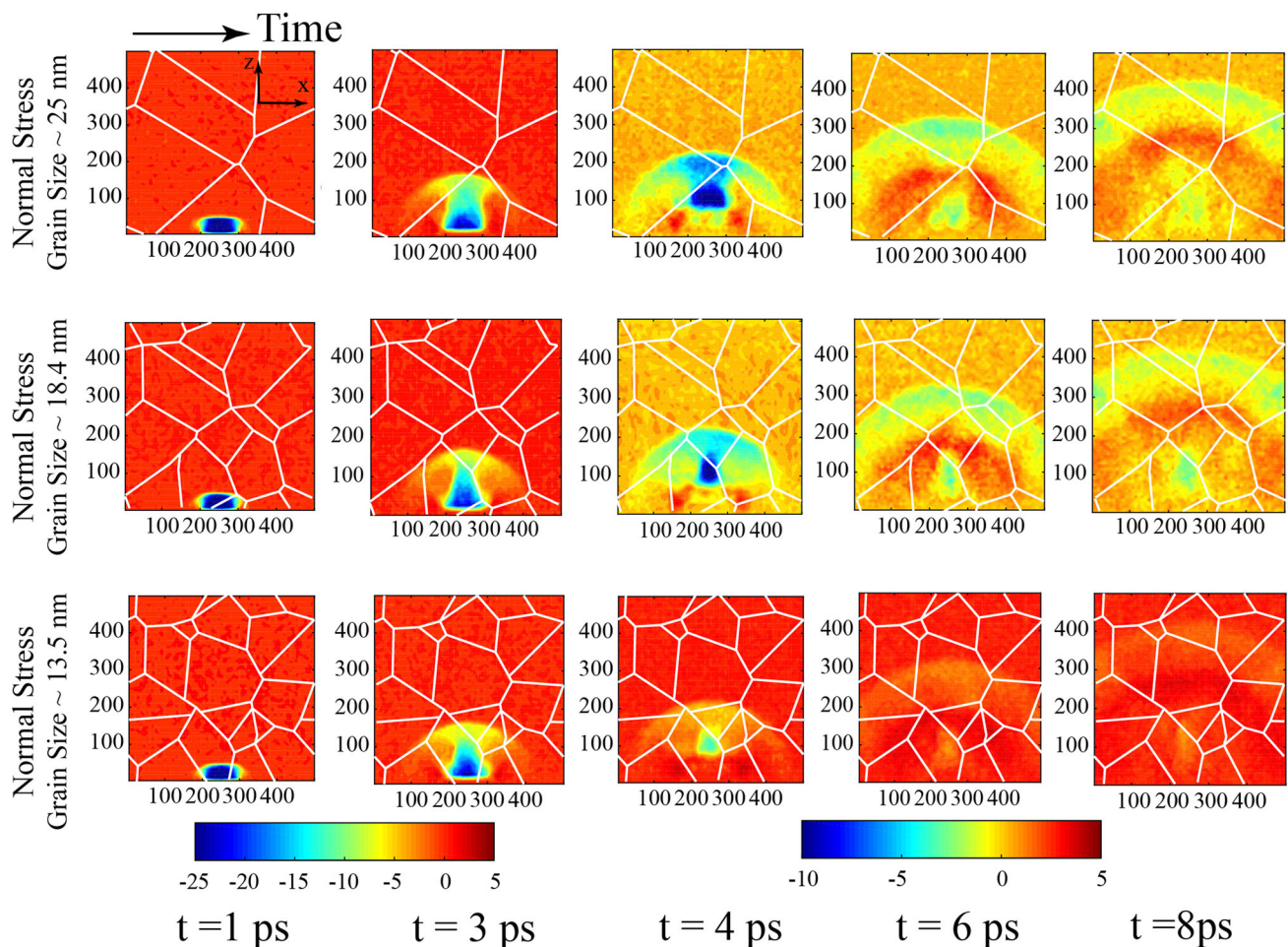


Fig. 7 Normal stress wave propagation in polycrystalline structures of NiTi for three different grain sizes: 13.5 nm, 18.4 nm, and 25 nm. The stress values in color bars are in GPa (Color figure online)

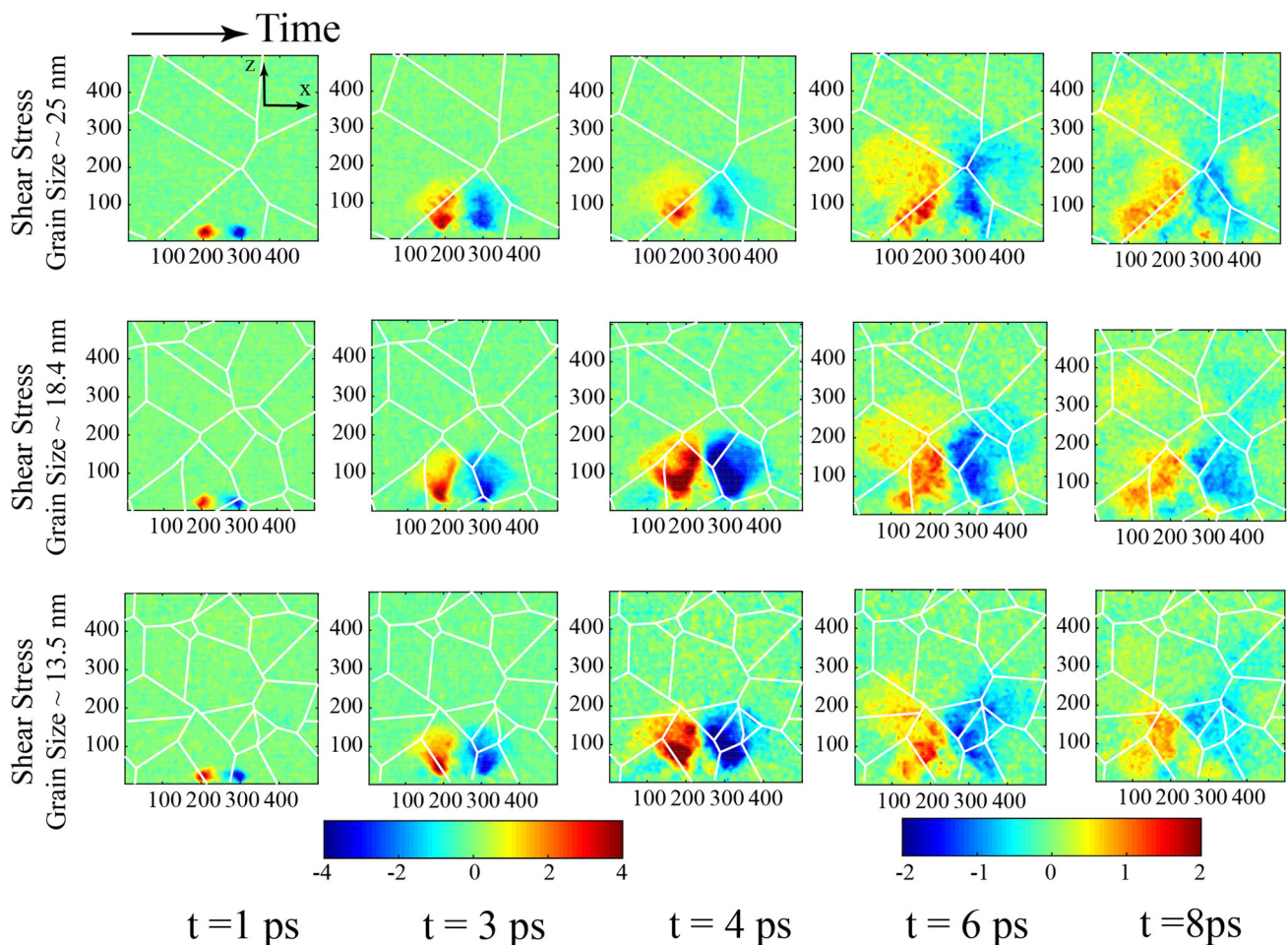


Fig. 8 Shear stress wave propagation in polycrystalline structures of NiTi for three different grain sizes: 13.5 nm, 18.4 nm, and 25 nm. The stress values in color bars are in GPa (Color figure online)

13 GPa). This high stress level propagates the phase transformation and plastic deformation through the bulks. Although from 1 ps to 3 ps some drop in the peak stress is observed, which could be due to energy dissipation through phase transformation and plastic deformation and also it could be due to presence of grain boundaries which act like an obstacle for shock stress wave. At the time of 4 ps and after that, the peak of elastic wave and phase transformation wave for the coarse grain are greater compared to the other grain sizes.

However, as discussed before, at the onset of unloading, another elastic wave with an opposite direction starts to propagate and at the time of 4 ps, this wave partially reaches the phase transformation peak and therefore, causes a significant drop in the stress level. This is why at the time of 5 ps the phase transformation peak drops below 5 GPa for all the grain sizes.

Figure 10 shows the maximum recorded stress values correspond to elastic wave front at different times and their corresponding positions over the length of the considered polycrystalline structures. The calculated stress values are

obtained from averaging over the cross sections of the middle cylinder along the loading direction same as single crystals. It can be seen that the coarse grain size overall shows the highest stress level and the fine grain size the lowest. In Fig. 10, the grain size 13.5 nm shows more decay in elastic wave front peak compared to the other polycrystalline structures. For instance, at the length of 100 Å from the surface on which the shock loading is applied, the stress in the grain size 13.5 nm drops under 10 GPa, while for the other two polycrystalline structures the stress level is still above 10 GPa. In addition, the grain sizes, 13.5 nm and 18.4 nm, show greater drop in inelastic wave front peak compared to the 25 nm. In the next section, the phase transformation propagation and plastic deformation in these polycrystalline structures will be discussed.

Phase Transformation Propagation

As it is mentioned before for an austenite NiTi to transform to a B19' martensite, there is a threshold in the equivalent

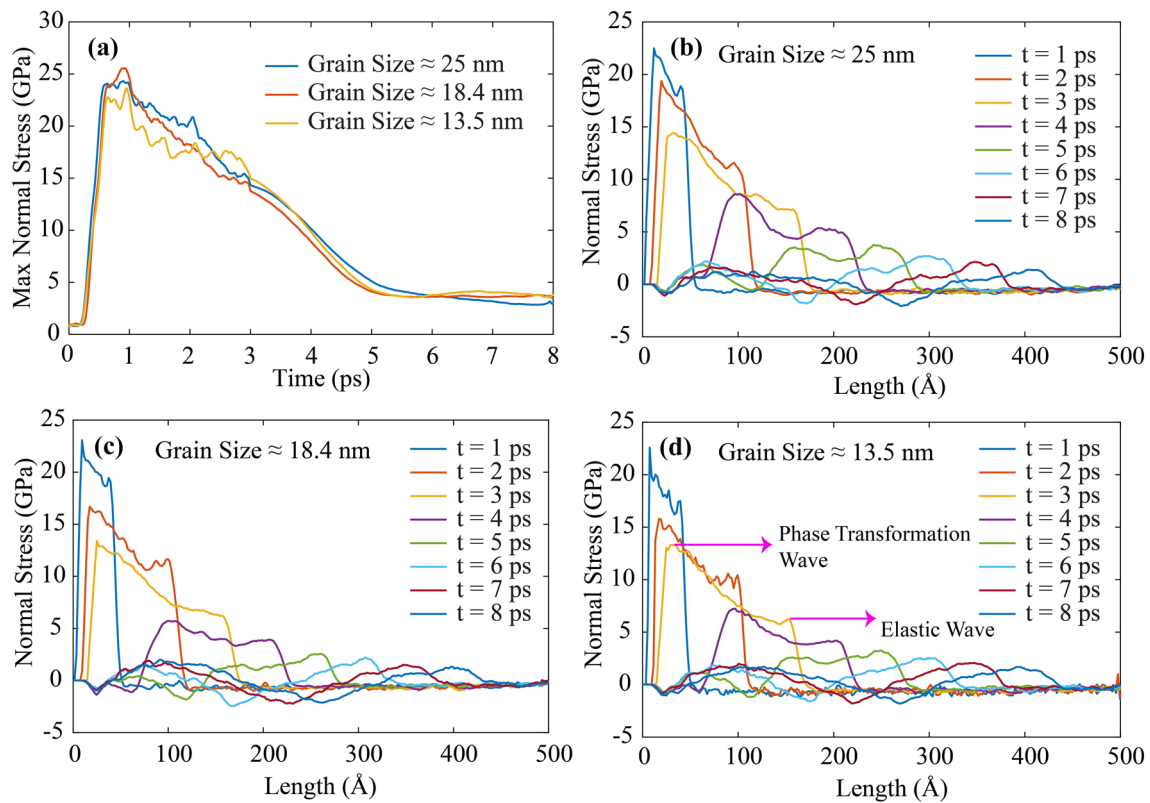


Fig. 9 a Maximum of normal stress wave during loading and propagation time for three polycrystalline structures with three different grain sizes: 13.5 nm, 18.4 nm, and 25 nm. **b** Normal stress

wave propagation for average grain size of 25 nm. **c** Normal stress wave propagation for average grain size of 18.4 nm. **d** Normal stress wave propagation for average grain size of 13.5 nm

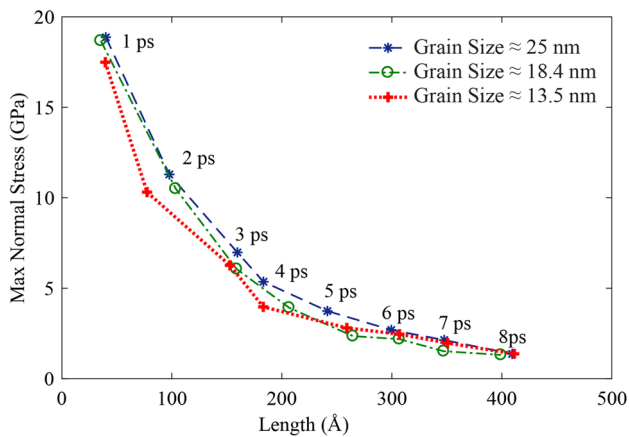
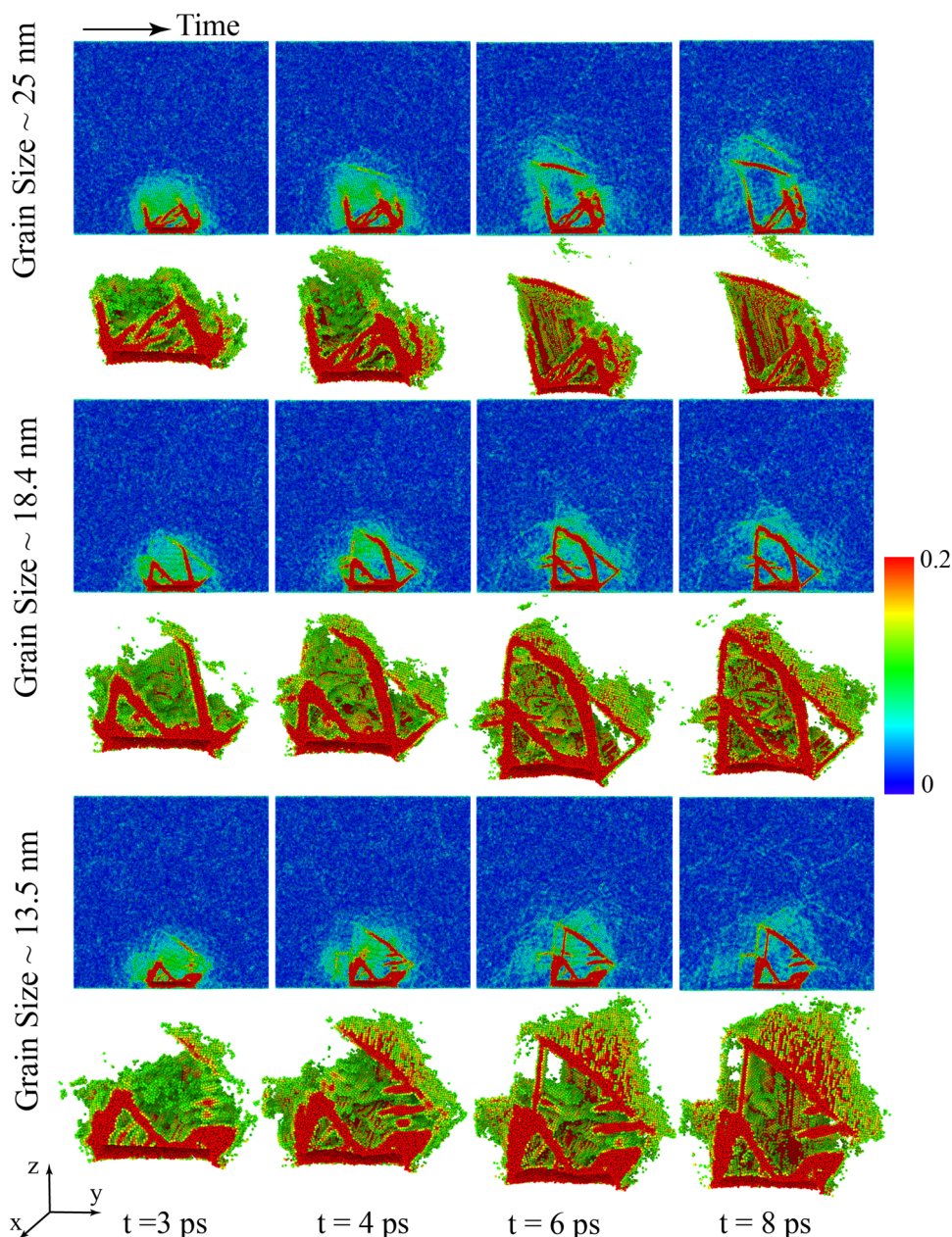


Fig. 10 Decay of normal stress wave for three polycrystalline structures with three different grain sizes: 13.5 nm, 18.4 nm, and 25 nm

Von Mises strain which is equal to 0.11. Above this strain threshold, the state of the material could be a combination of phase transformation and plastic deformation. The Von Mises strain propagation for the three polycrystalline NiTis with different grain sizes are shown in Fig. 11. This parameter shows both phase transformation and plastic deformation propagation. At the time of 8 ps, which is 5 ps

after removing the shock loading, some of the regions with phase transformation are recovered back to austenite. More time is needed to capture all the regions in which all the phase transformation is recovered in the structures. However, it is not possible in practice due to the computational restrictions. In order to solve this problem in the next section, we propose a method to distinguish the regions with plastic deformation and phase transformation in the single- crystal and polycrystalline NiTi alloys. It can be seen in Fig. 11 that the size of phase transformed regions decrease by reducing the size of grains in polycrystalline structures. As it is expected, grain boundaries volume fraction increases when the grain sizes decrease and these grain boundaries as obstacles prevent the phase transformation propagation in the polycrystalline structures. It can be seen that the phase transformation and plastic deformations initiate at the loading region and they start to propagate but they are stopped when reaching the grain boundaries. Also, the pattern of phase transformation shows that when the phase transformation and plastic deformation reach the grain boundaries they prefer to propagate through the boundaries, over penetrating to the neighbor grain. Since, grain boundaries are kind of defects in the structure and they are a summation of several

Fig. 11 Von Mises shear strain parameter which shows phase transformation propagation and plastic deformation in three different polycrystalline structures under shock loading. Von Mises shear strain values 0 and 0.11 correspond to regions with austenite and martensite phases, respectively. The values between 0.11 and 0.2 show regions with combined phase transformation and plastic deformation



dislocations, they could trigger the plastic deformation and phase transformation propagation and deploy them to propagate through the boundaries.

Interaction Between Plastic Deformation and Phase Transformation

In this section, two methods are used to distinguish the plastic deformation and phase transformation due to shock loading in NiTi single crystal $x : [100]y : [010]z : [001]$, which is selected as a representative direction.

In the first method, after applying the shock load for 3 ps, the load is removed and the structure is relaxed for

enough time (200 ps). During this relaxation time a reverse phase transformation happens in martensite regions with no plastic deformation, and the material transforms back to austenite, while plastic deformations remain in the structure. It is worth noting that in addition to the remained plastic deformation, even after a long time of relaxing the structure once the load is removed, some defects in the structure, including dislocations and grain boundaries, might prevent the reverse phase transformation in some regions of the material. Studying the interaction between the defects and reverse phase transformation is the subject of a future communication by the authors [1, 56]. However, in this work, this effect is ignored with an acceptable accuracy since the fraction of such regions is not significant.

Fig. 12 **a** Single crystal of NiTi with crystal orientations of [100][010][001]. **b–d** Plastically deformed region on x - z planes at $y = 200, 250,$ and 300 \AA . **e** Overlaid plastically deformed regions. **f** Plastically deformed region from theory of plasticity

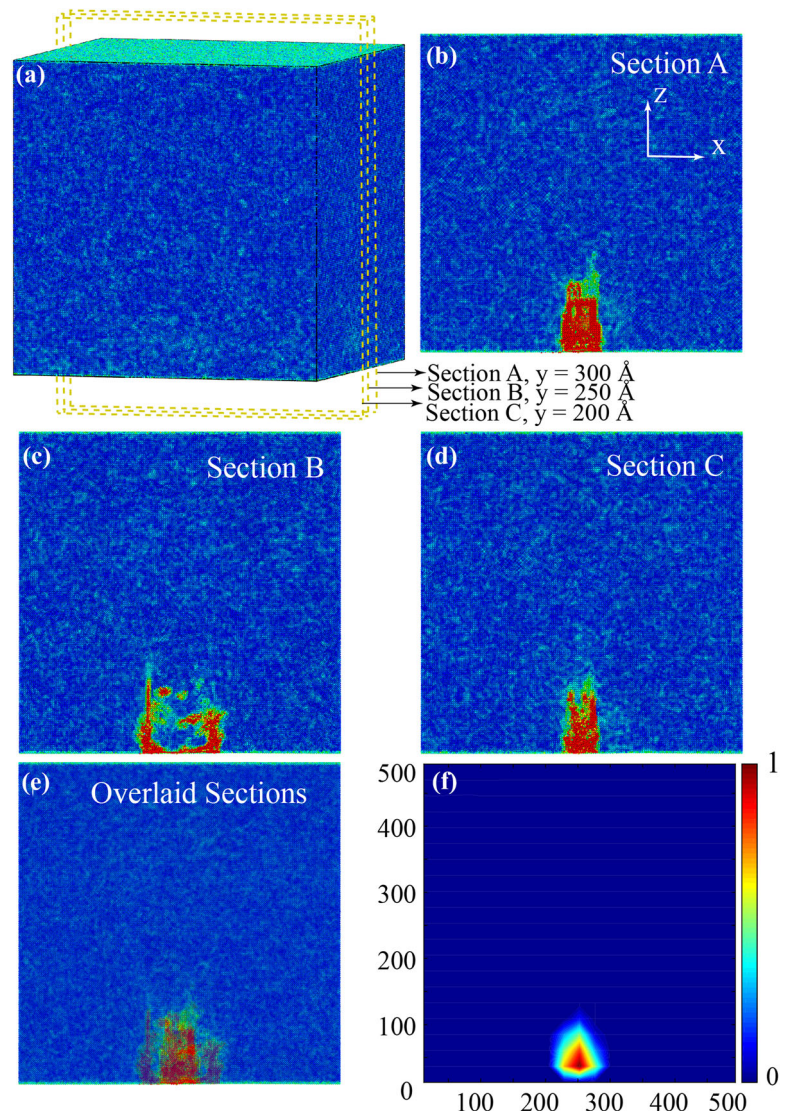


Figure 12a shows the single crystal under shock loading. It is worth noting that the load is applied on a circle (with its center at $x = y = 250 \text{ \AA}$) on the lower surface. Three sections A, B and C are shown in this figure which correspond to the beginning, middle and the end of loading regions. The permanently deformed regions are illustrated at these three sections in Fig. 12b–d, respectively. The overlaid sections which shows all the permanently deformed regions is shown in Fig. 12e. In the second method, we consider the most favorable slip systems of a B2 NiTi alloy structure [57, 58]. These slip systems and the corresponding critical stress values are expressed in Table 1 [57]:

The shear stress in these slip planes are calculated every 0.1 ps for the total time of simulation and in each slip system which shear stress reaches the critical value, slip happens and the corresponding region is assumed to experience a plastic deformation which is permanently deformed. Figure 12f shows the superposition of those

Table 1 Critical shear stress values of B2 NiTi alloys in austenite phase for the (011)[100] and (011)[111] slip systems

Slip plane	Slip direction	$(\tau_{\text{Shear}})_{\text{Critical}}$ (GPa)
(011)	[100]	0.71
(011)	[111]	1.2

permanently deformed regions. This contour plot also illustrates the intensity of the slippage during the time of simulation which means the red colored areas show those regions that the slip systems were activated more than once during the time of simulations. Comparing Fig. 12e and f, it can be seen that there is a good agreement between the two methods. We could say that in order to detect and distinguish the plastic deformation and phase transformation in the NiTi structures under shock loading, we could

use the second proposed method since it is computationally cost effective.

Conclusions

In this paper, the energy dissipation and the phase transformation caused by the stress wave propagation in single-crystal and polycrystalline austenite NiTi alloys under shock wave loadings are investigated. Molecular dynamics (MD) simulations are utilized as a superior method to study the effect of microstructures such as lattice orientations, grain sizes and grain boundaries on the patterns of stress wave and phase transformation initiation and propagation at the atomistic level in NiTi alloys. A criterion based on equivalent shear strains is used to detect the inelastic deformation in the NiTi structures. This parameter is used to detect the regions with martensitic phase transformation and plastic deformation. Regions with phase transformation and plastic deformation in the structures are distinguished by implementing two proposed methods. It is expected to observe the dissipated energy in NiTi structures being caused by both phase transformation and plastic deformation. The next step would be calculating the total energy dissipated during the stress wave propagation, and finding the contribution of phase transformation in the dissipated energy compared to the energy which is dissipated by the plastic deformation in the material. This will be the topic of a future communication by the authors, where a method will be proposed to quantify the dissipated energy due to the phase transformation in NiTi alloys under shock loading.

Acknowledgements R. M. acknowledges support from the Air Force Office of Scientific Research under Award Number FA9550-18-1-0169. The authors acknowledge Advanced Research Computing at Virginia Tech for providing computational resources and technical support that have contributed to the results reported within this paper. <http://www.arc.vt.edu>.

References

1. Yazdandoost F, Mirzaeifar R (2017) Tilt grain boundaries energy and structure in NiTi alloys. *Comput Mater Sci* 131:108–119
2. Chowdhury P, Ren G, Sehitoglu H (2015) NiTi superelasticity via atomistic simulations. *Philos Mag Lett* 95:1–13
3. Cui J, Chu YS, Famodu OO, Furuya Y, Hattrick-Simpers J, James RD, Ludwig A, Thienhaus S, Wuttig M, Zhang Z (2006) Combinatorial search of thermoelastic shape-memory alloys with extremely small hysteresis width. *Nat Mater* 5(4):286–290
4. Hartl DJ, Lagoudas DC (2007) Aerospace applications of shape memory alloys. *Proc Inst Mech Eng Part G* 221(4):535–552
5. DesRoches R, Delemont M (2002) Seismic retrofit of simply supported bridges using shape memory alloys. *Eng Struct* 24(3):325–332
6. DesRoches R, Smith B (2004) Shape memory alloys in seismic resistant design and retrofit: a critical review of their potential and limitations. *J Earthq Eng* 8:415–429
7. Lagoudas DC, Ravi-Chandar K, Sarh K, Popov P (2003) Dynamic loading of polycrystalline shape memory alloy rods. *Mech Mater* 35(7):689–716
8. Mirzaeifar R, DesRoches R, Yavari A (2011) A combined analytical, numerical, and experimental study of shape-memory-alloy helical springs. *Int J Solids Struct* 48(3–4):611–624
9. Chowdhury P, Patriarca L, Ren G, Sehitoglu H (2016) Molecular dynamics modeling of NiTi superelasticity in presence of nanoprecipitates. *Int J Plast*. <https://doi.org/10.1016/j.ijplas.2016.01.011>
10. Sehitoglu H, Hamilton R, Maier H, and Chumlyakov Y (2004) Hysteresis in NiTi alloys. In: *Journal de Physique IV (Proceedings)*. EDP sciences
11. DesRoches R, Taftali B, Ellingwood BR (2010) Seismic performance assessment of steel frames with shape memory alloy connections. Part I analysis and seismic demands. *J Earthq Eng* 14(4):471–486
12. DesRoches BAR (2007) Effect of hysteretic properties of superelastic shape memory alloys on the seismic performance of structures. *Struct Control Health Monit* 14:301–320
13. Nemat-Nasser S, Choi JY, Guo W-G, Isaacs JB, Taya M (2005) High strain-rate, small strain response of a NiTi shape-memory alloy. *J Eng Mater Technol* 127(1):83–89
14. Yin Q, Wu X, Huang C (2017) Atomistic study on shock behaviour of NiTi shape memory alloy. *Phil Mag* 97(16):1311–1333
15. Lagoudas DC, Popov P (2003) Numerical studies of wave propagation in polycrystalline shape memory alloy rods. *Smart Struct Mater* 2003(5053):294–304
16. Liao Y, Ye C, Lin D, Suslov S, Cheng GJ (2012) Deformation induced martensite in NiTi and its shape memory effects generated by low temperature laser shock peening. *J Appl Phys* 112(3):033515
17. Millett J, Bourne N (2004) The shock-induced mechanical response of the shape memory alloy, NiTi. *Mater Sci Eng A* 378(1):138–142
18. Thakur A, Thadhani N, Schwarz R (1997) Shock-induced martensitic transformations in near-equiatomic NiTi alloys. *Metall Mater Trans A* 28(7):1445–1455
19. Millett J, Bourne N, Gray G III (2002) Behavior of the shape memory alloy NiTi during one-dimensional shock loading. *J Appl Phys* 92(6):3107–3110
20. Meziere Y, Millett J, Bourne N (2006) Equation of state and mechanical response of NiTi during one-dimensional shock loading. *J Appl Phys* 100(3):033513
21. Razorenov SV, Garkushin GV, Kanel GI, and Popov NN (2009) Shock-wave response of NiTi shape memory alloys in the transformation temperature range. In: *AIP Conference Proceedings*. AIP
22. Millett J, Bourne N, Gray III G, and Stevens G (2002) On the shock response of the shape memory alloy, NiTi. In: *AIP Conference Proceedings*. AIP
23. Yuan F, Wu X (2012) Shock response of nanotwinned copper from large-scale molecular dynamics simulations. *Phys Rev B* 86(13):134108
24. Arman B, Luo S-N, Germann TC, Çağın T (2010) Dynamic response of Cu 46 Zr 54 metallic glass to high-strain-rate shock loading: plasticity, spall, and atomic-level structures. *Phys Rev B* 81(14):144201
25. Bringa E, Rosolankova K, Rudd R, Remington B, Wark J, Duchaineau M, Kalantar D, Hawreliak J, Belak J (2006) Shock deformation of face-centred-cubic metals on subnanosecond timescales. *Nat Mater* 5(10):805–809

26. Zhao F, Li B, Jian W, Wang L, Luo S (2015) Shock-induced melting of honeycomb-shaped Cu nanofoams: effects of porosity. *J Appl Phys* 118(3):035904
27. Jiang S, Sewell TD, Thompson DL (2016) Molecular dynamics simulations of shock wave propagation through the crystal-melt interface of (100)-oriented nitromethane. *J Phys Chem C* 120(40):22989–23000
28. Kadau K, Germann TC, Lomdahl PS, Holian BL (2002) Microscopic view of structural phase transitions induced by shock waves. *Science* 296(5573):1681–1684
29. Luo S-N, Germann TC, Desai TG, Tonks DL, An Q (2010) Anisotropic shock response of columnar nanocrystalline Cu. *J Appl Phys* 107(12):123507
30. Luo S-N, Germann TC, Tonks DL, An Q (2010) Shock wave loading and spallation of copper bicrystals with asymmetric Σ 3<110> tilt grain boundaries. *J Appl Phys* 108(9):093526
31. Ma W, Zhu W, Jing F (2010) The shock-front structure of nanocrystalline aluminum. *Appl Phys Lett* 97(12):121903
32. Sichani MM, Spearot DE (2015) A molecular dynamics study of the role of grain size and orientation on compression of nanocrystalline Cu during shock. *Comput Mater Sci* 108:226–232
33. Wang JJ and Guo WG (2012) Pseudo-elastic behavior of NiTi SMA under the quasi-static and the impact cyclic tests. In: *Advanced materials research*. Trans Tech Publ
34. Razorenov S, Garkushin G, Kashin O, Ratochka I (2011) Behavior of the Nickel–Titanium alloys with the shape memory effect under conditions of shock wave loading. *Phys Solid State* 53(4):824–829
35. Chen WW, Wu Q, Kang JH, Winfree NA (2001) Compressive superelastic behavior of a NiTi shape memory alloy at strain rates of 0.001–750 s⁻¹. *Int J Solids Struct* 38(50–51):8989–8998
36. Niemczura J, Ravi-Chandar K (2006) Dynamics of propagating phase boundaries in NiTi. *J Mech Phys Solids* 54(10):2136–2161
37. Zhang X, Tang Z (2010) Experimental study on the dynamic behavior of TiNi cantilever beams with rectangular cross-section under transversal impact. *Int J Impact Eng* 37(7):813–827
38. Bekker A, Jimenez-Victory JC, Popov P, Lagoudas DC (2002) Impact induced propagation of phase transformation in a shape memory alloy rod. *Int J Plast* 18:1447–1479
39. Zurbitu J, Castillo G, Urrutibeascoa I, Aurrekoetxea J (2009) Low-energy tensile-impact behavior of superelastic NiTi shape memory alloy wires. *Mech Mater* 41(9):1050–1058
40. Saletti D, Pattofatto S, Zhao H (2013) Measurement of phase transformation properties under moderate impact tensile loading in a NiTi alloy. *Mech Mater* 65:1–11
41. Zurbitu J, Kustov S, Zabaleta A, Cesari E, and Aurrekoetxea J (2010) Thermo-mechanical behaviour of NiTi at impact. In: *Shape memory alloys*. InTech
42. Chen Y, Lagoudas DC (2005) Wave propagation in shape memory alloy rods under impulsive loads. *Proc Royal Soc A* 461(2064):3871–3892
43. Sadeghi O, Bakhtiari-Nejad M, Yazdandoost F, Shahab S, Mirzaeifar R (2018) Dissipation of cavitation-induced shock waves energy through phase transformation in NiTi alloys. *Int J Mech Sci* 137:304–314
44. Lai W, Liu B (2000) Lattice stability of some NiTi alloy phases versus their chemical composition and disordering. *J Phys* 12(5):L53
45. Zhong Y, Gall K, Zhu T (2011) Atomistic study of nanotwins in NiTi shape memory alloys. *J Appl Phys* 110(3):033532
46. Zhong Y, Gall K, Zhu T (2012) Atomistic characterization of pseudoelasticity and shape memory in NiTi nanopillars. *Acta Mater* 60(18):6301–6311
47. Lai WS, Liu BX (2000) Lattice stability of some NiTi alloy phases versus their chemical composition and disordering. *J Phys* 12(5):L53
48. Plimpton S (1995) Fast parallel algorithms for short-range molecular dynamics. *J Comput Phys* 117(1):1–19
49. Stukowski A (2009) Visualization and analysis of atomistic simulation data with OVITO—the open visualization tool. *Modell Simul Mater Sci Eng* 18(1):015012
50. Boots BN (1982) The arrangement of cells in random networks. *Metallography* 15(1):53–62
51. Brill T, Mittelbach S, Assmus W, Mullner M, Luthi B (1991) Elastic properties of NiTi. *J Phys* 3(48):9621
52. Lane C (2014) Wave propagation in anisotropic media. In: *The development of a 2D ultrasonic array inspection for single crystal turbine blades*. Springer: Cham. p. 13–39
53. Huang XY, Ackland GJ, Rabe KM (2003) Crystal structures and shape-memory behaviour of NiTi. *Nat Mater* 2(5):307–311
54. Shimizu F, Ogata S, Li J (2007) Theory of shear banding in metallic glasses and molecular dynamics calculations. *Mater Trans* 48(11):2923–2927
55. Qin S-J, Shang J-X, Wang F-H, Chen Y (2018) Symmetrical tilt grain boundary engineering of NiTi shape memory alloy: an atomistic insight. *Mater Des* 137:361–370
56. Yazdandoost F, Mirzaeifar R (2017) Generalized stacking fault energy and dislocation properties in NiTi shape memory alloys. *J Alloy Compd* 709:72–81
57. Wang J, Sehitoglu H, Maier H (2014) Dislocation slip stress prediction in shape memory alloys. *Int J Plast* 54:247–266
58. Ezaz T, Wang J, Sehitoglu H, Maier H (2013) Plastic deformation of NiTi shape memory alloys. *Acta Mater* 61(1):67–78